crystals

MDPI

Article

Al/Graphene Co-Doped ZnO Electrodes: Impact on CTS Thin-Film Solar Cell Efficiency

Done Ozbek [1], Meryem Cam [1], Guldone Toplu [1], Sevde Erkan [1], Serkan Erkan [1], Ali Altuntepe [2,*], Kasim Ocakoglu [3], Sakir Aydogan [4], Yavuz Atasoy [1,5], Mehmet Ali Olgar [1,6] and Recep Zan [1,6,*]

1 Nanotechnology Application and Research Center, Niğde Ömer Halisdemir University, Nigde 51200, Türkiye; done_ozbek@mail.ohu.edu.tr (D.O.); meryem_cam@mail.ohu.edu.tr (M.C.); guldone_toplu@mail.ohu.edu.tr (G.T.); sevde.erkan@mail.ohu.edu.tr (S.E.); srknerkan25@ku.edu.tr (S.E.); yavuzatasoy@ohu.edu.tr (Y.A.); mehmetaliolgar@ohu.edu.tr (M.A.O.)
2 Optical Excellence Application and Research Center, Sivas University of Science and Technology, Sivas 58000, Türkiye
3 Department of Engineering Fundamental Sciences, Faculty of Engineering, Tarsus University, Tarsus 33400, Türkiye; kasim.ocakoglu@tarsus.edu.tr
4 Department of Physics, Science Faculty, Atatürk University, Erzurum 25240, Türkiye; saydogan@atauni.edu.tr
5 Niğde Zübeyde Hanım Vocational School of Health Services, Niğde Ömer Halisdemir University, Nigde 51200, Türkiye
6 Department of Physics, Niğde Ömer Halisdemir University, Nigde 51200, Türkiye
* Correspondence: alialtuntepe@sivas.edu.tr (A.A.); recep.zan@ohu.edu.tr (R.Z.)

Abstract

This study investigates pristine and doped ZnO thin films fabricated via the sol-gel technique, aiming to address efficiency challenges when used as transparent conductive oxide (TCO) layers in thin-film solar cells. ZnO was first doped with aluminum (Al), and subsequently with both Al and reduced graphene oxide (rGO), to evaluate the individual and combined effects of these dopants. The optimal pH value for the ZnO structure was initially determined, with the film produced at pH 9 exhibiting the most favorable characteristics. Al doping was then optimized at a ratio of Al/(Al + Zn) = 0.2, followed by optimization of the graphene content at 1.5 wt%. In this context, the structural, optical, and electrical properties of pristine ZnO, Al-doped ZnO (AZO), and Al and graphene co-doped ZnO (Gr:AZO) thin films were systematically investigated. These films were integrated as TCO layers into Cu_2SnS_3 (CTS)-based thin-film solar cells fabricated via physical vapor deposition (PVD). The cell architecture employed an 80 nm pristine ZnO window layer, while the doped ZnO films (300 nm) served as TCO layers. To assess the influence of the chemically deposited top layers, device performance was compared against a reference cell in which all layers were fabricated entirely using PVD. As expected, the reference cell exhibited superior performance compared to the cell whose AZO layer deposited chemically; however, the incorporation of both Al and graphene significantly enhanced the efficiency of the chemically modified cell, outperforming devices using only pristine or singly doped ZnO films. These results demonstrate the promising potential of co-doped solution-processed ZnO films as an alternative TCO layer in improving the performance of thin-film solar cell technologies.

Keywords: ZnO; AZO; graphene; CTS; thin film; solution-based solar cell

Check for updates

Academic Editor: Gu Xu

Received: 22 December 2025
Revised: 6 January 2026
Accepted: 13 January 2026
Published: 17 January 2026

Copyright: © 2026 by the authors. Licensee MDPI, Basel, Switzerland. This article is an open access article distributed under the terms and conditions of the Creative Commons Attribution (CC BY) license.

1. Introduction

Transparent conductive oxide (TCO) materials are recognized for a combination of beneficial properties: high transparency, non-toxicity, and chemical stability [1]. Due

to these properties, they are widely used in various fields such as solar cells [2], laser diodes [3], ultraviolet lasers [4], thin-film transistors [5], optical detectors [6], and light-emitting diodes [7]. Among those oxide-based materials, indium-doped tin oxide (ITO) is the most commonly used TCO layer thanks to its superior electrical and optical properties. However, despite its advantages, ITO has several drawbacks, including its brittle nature and the limited reserves of indium, which drive its cost too high. [8]. For these reasons, zinc oxide (ZnO) has emerged as a promising alternative TCO material due to the fact that it consists of elements from group II-VI that are earth-abundant, cost-effective and environmentally friendly [9].

Studies have shown that variations in production methods lead to changes in such features as crystal structure, surface morphology, and electrical and optical properties of both undoped and doped ZnO thin films. For this, a variety of methods are employed to produce ZnO-based thin films. Physical methods for obtaining these films include thermal evaporation [10], pulsed laser deposition (PLD) [11], magnetron sputtering [12], and electron beam evaporation (e-beam) [13]. On the other hand, chemical methods encompass spray pyrolysis [14], spin coating [15], electrodeposition [16], and chemical vapor deposition (CVD) [17]. Among these techniques, spin coating is notable for being a low-cost, simple, and rapid production method.

It is well known that various growth parameters including chemical composition, annealing temperature, and duration have significant effects on the properties of ZnO thin films produced by chemical methods, particularly spin coating. One of the factors influencing the quality of ZnO films is the pH value of the prepared solution. Studies suggest that optimizing the solution pH enables control over the grain size, shape, and density of the films, resulting in improved film quality and performance of ZnO-based devices [18]. To illustrate, Abdulrahman et al. achieved high-quality ZnO nanostructures using a low-temperature, modified chemical bath deposition method with pH levels varied from 6 to 12. They found that increasing pH enhanced the transmittance of ZnO nanostructures, but while high crystal quality was maintained up to pH 9.4, further increases caused deterioration. Based on structural and optical properties, the researchers determined pH 6.7 to be optimal for these ZnO nanostructures [19]. In another study, Meziane et al. investigated the deposition of ZnO thin films via spin coating, using solutions with pH systematically varied from 6.5 to 10.5 in 0.5-unit increments. Their analyses revealed that crystal quality and grain size improved up to pH 9.5, where the sample exhibited a resistivity of 1.7×10^{-1} Ωcm and a carrier concentration of 1.3×10^{20} cm^{-3}, leading them to identify this pH as optimal [20]. However, there have been limited works focused on the effect of pH, which is used over a wide range, on the fundamental properties of ZnO thin films.

Additionally, ZnO is an n-type semiconductor material with a wide band gap of 3.37 eV [21] and a high exciton binding energy of 60 meV [22]. However, pristine ZnO is commonly classified as a weak n-type conductivity due to its limited inherent zinc interstitials and oxygen vacancies [23]. Various approaches have been proposed to overcome the conductivity issues in ZnO. One of the methods to enhance carrier concentration is creating oxygen vacancies, introducing excess Zn atoms or extrinsic doping. Overall, the extrinsic doping strategy is more controllable than altering vacancies and/or interstitials in ZnO [24]. In this context, elements from group IIIA, such as aluminum (Al), gallium (Ga), and indium (In), are mostly preferred for extrinsic doping [25]. The incorporation of these dopants acts as shallow donors by providing additional free electrons, reflecting proper/higher electrical conductivity compared to undoped ZnO. Among these elements, Al is particularly favored as a dopant due to its abundance, lower cost, and non-toxic nature when compared to Ga and In [26]. In addition to this, aluminum-doped zinc oxide (AZO)

thin films are prominent among TCO materials, exhibiting both high optical transparency and good electrical conductivity. Although the ionic radius difference between Zn^{2+} and Al^{3+} causes some lattice distortion and crystal defects in AZO films [27], the relatively small difference in atomic radii helps to minimize these defects [28]. Furthermore, ZnO was also co-doped with different metals. For example, H. Saadi et al. investigated the effects of Fe and Al co-doping on ZnO. Their results demonstrated that co-doping led to a reduction in crystallite size, while the electrical conductivity increased significantly. This enhancement in electrical conductivity indicated that Fe-Al co-doped ZnO becomes more suitable than intrinsic ZnO for optoelectronic applications [29].

Graphene, fundamentally defined as a two-dimensional arrangement of carbon atoms in a hexagonal honeycomb lattice, possesses exceptional properties such as high electrical and thermal conductivity [30], outstanding mechanical strength, high electron mobility, and excellent optical transmittance [31]. In recent years, research on the incorporation of Graphene (Gr) into ZnO films has gained momentum. It is well known that graphene doping enhances electrical conductivity by allowing carbon atoms to occupy vacancies within the ZnO structure [32]. In a study conducted by Ian et al., it was reported that by incorporating reduced graphene oxide (rGO) into aluminum-doped ZnO (AZO) via the sol-gel deposition method, the film's resistance could be reduced without a significant decrease in optical transmittance [33]. Yet, studies on the fabrication and characterization of graphene-doped ZnO thin films for solar cell applications remain limited.

In this context, the present study aims to fabricate solution-based undoped ZnO, Al-doped ZnO (AZO), and graphene-doped AZO (Gr:AZO) thin films under optimized conditions, including pH value and the concentrations of Al and graphene. These films were then being integrated into Cu_2SnS_3 (CTS) thin-film-based solar cells to evaluate their effects on device performance. A solar cell structure composed of Glass/Mo/CTS/CdS/ZnO/AZO(Gr)/Ag was fabricated based on the optimized conditions for ZnO and AZO layers. The solar cell performance was compared with that of a reference cell whose top layers are entirely fabricated using a PVD system, in order to investigate the impact of the chemically deposited layers on device performance. Overall, this study aims to develop a TCO layer with high transparency and to enhance cell efficiency through an environmentally friendly and cost-effective approach.

2. Experimental Section

In this study, the sol-gel method was used to produce undoped, Al-doped ZnO and graphene-doped AZO thin films. Before the coating process, the glass substrates were cleaned using an ultrasonic cleaner with acetone, isopropanol, and deionized water for 5, 5 and 10 min, respectively, followed by drying with nitrogen (N_2) gas. Finally, to minimize potential contamination, the substrates were exposed to argon plasma for 15 min. Zinc acetate dihydrate ($Zn(CH_3COO)_2{\cdot}2H_2O$) was utilized as the ZnO precursor, aluminum nitrate nonahydrate ($Al(NO_3)_3{\cdot}9H_2O$) as the aluminum dopant, citric acid ($C_6H_8O_7{\cdot}H_2O$) as the binder, 2-methoxyethanol ($C_3H_8O_2$) as the solvent, and ethanolamine (C_2H_7NO) as the stabilizer. The ZnO solution was prepared by combining two separate solutions. First, 1.10 g (5 mmol) of zinc acetate dihydrate and 0.96 g (5 mmol) citric acid were separately dissolved in 2-methoxyethanol at room temperature by stirring on a magnetic stirrer for 1 h. Then, the citric acid solution was added dropwise to the zinc solution, which was heated to 75 °C. Finally, ethanolamine was added until the pH values of the solutions reached 2, 7, 9, and 12, and the mixture was stirred for 12 h. The concentration of the solutions was set to 0.25 M.

In the second phase, the effect of pH on ZnO thin films was examined. A pH value of 9, which suggested the superior features, was then used to prepare AZO solutions.

Zinc acetate dihydrate, citric acid and aluminum nitrate non-hydrate were dissolved in 2-methoxyethanol for 1 h. The citric acid and aluminum solutions were then added dropwise to the zinc solution on a heating plate set at 75 °C. The aluminum content was adjusted to achieve Al/(Al + Zn) molar ratios of 10%, 15%, and 20% by adding 0.2084 g, 0.3310 g, and 0.4689 g of aluminum nitrate nonahydrate, respectively. Ethanolamine was added until the pH reached 9, and the mixture was stirred on the heating plate for 12 h in order to obtain a homogeneous and clear solution.

In the final stage, graphene powder obtained via the liquid phase exfoliation method was added to the solution containing 15% Al, which had previously demonstrated the most favorable properties. Graphene was incorporated into the solution at weight percentages of 0.5%, 1%, 1.5%, and 2%, corresponding to mass amounts of 5.5 mg, 11.0 mg, 16.5 mg, and 22.0 mg, respectively. To ensure uniform dispersion of graphene within the solution, the mixtures were subjected to ultrasonic treatment in a bath for one hour, resulting in homogeneous colloidal solutions.

The prepared undoped ZnO, Al-doped ZnO and graphene-doped ZnO solutions were coated onto glass substrates using a spin-coating system. The coating process was performed at a spin speed of 4000 rpm for 40 s. To achieve the desired thickness, the process was repeated several times to obtain ZnO films of approximately 80 nm thickness and AZO films of approximately 300 nm thickness. After each cycle, the films were subjected to a pre-annealing process on a heating plate at 200 °C for 10 min to enhance adhesion to the substrates. After completing the coating process, ZnO films were annealed in air at 300 °C for 10 min. This step was performed to induce crystallization and evaluate the effect of pH on the films.

After determining the optimal doping ratio, molybdenum (Mo) back contact and CTS absorber layer were deposited on glass substrates using a PVD system, based on previously optimized parameters by our research team [34]. A Mo thin film, approximately 250 nm thick, was deposited onto a glass substrate using a DC sputtering power source. This Mo film serves as the back electrical contact for the solar cell device, upon which it will be built. Then, the CTS absorber layer was produced on Mo-coated glass substrates using a two-step method. First, Cu and Sn layers were sequentially deposited using DC and RF magnetron sputter sources with high-purity targets, respectively. Metallic layer depositions were carried out at a base pressure of approximately 2.10^{-6} torr and a deposition pressure of 3.10^{-3} Torr. The deposited Cu/Sn/Cu metallic stack was annealed in a graphite box under sulfur vapor pressure using high-purity sulfur powder (10 mg), resulting in the CTS thin film. The n-type CdS layer, with a thickness of 80 nm, was deposited on the CTS layer using the chemical bath deposition (CBD) method, forming the Glass/Mo/CTS/CdS structure. Subsequently, an 80 nm thick ZnO buffer layer and a 300 nm thick AZO layer were deposited using a spin coating system with the optimized growth process. For comparison, the same cell structure was fabricated with ZnO and AZO layers, which were deposited by RF magnetron sputtering in the PVD system. Finally, silver contacts were deposited onto the layers forming the completed Glass/Mo/CTS/CdS/ZnO/AZO/Ag cell structures.

Several characterization methods were employed for the produced CTS, pristine and doped ZnO thin films. Structural analyses of the samples grown at different pH values were conducted usingX-ray Diffraction (XRD) (Malvern Panalytical Empyrean, Almelo, The Netherlands) with CuKα radiation (λ = 1.15406 Å). The optical properties of the films were analyzed using an Ellipsometer (J.A. Woollam-VASE, Lincoln, NE, USA) in the 300–1200 nm range at room temperature. Energy Dispersive X-ray Spectroscopy (EDX) (Ematek EDAX, West Orange, NJ, USA) at a beam voltage of 20 kV was used to determine the atomic ratios of constituent elements in the samples. Electrical parameters of the samples were

determined using the Hall Effect (Ecopia HMS-3000, Anyang-si, Gyeonggi, Republic of Korea) measurement system. The current density and voltage (J-V) measurements of the fabricated solar cells were conducted under 100 mW/cm^2 illumination, using a calibrated solar simulator with an active area of approximately 1 cm^2.

3. Results and Discussion

3.1. XRD

The crystal structure of ZnO thin films grown using solutions prepared at pH values of 2, 7, 9, and 12 was characterized by XRD. The XRD spectrum of ZnO thin films is shown in Figure 1a. According to the figure, all samples exhibit a hexagonal wurtzite structure with prominent peaks approximately at 31.77°, 34.42°, 36.26°, 47.55°, 56.66°, 62.90°, 67.96°, and 69.15°, corresponding to the (100), (002), (101), (102), (110), (103), (112), and (201) preferred orientations, respectively (JCPDS: 98-016-2843). The expanded view of the three dominant peak variations with respect to pH value is shown in Figure 1b. It can be observed that the sample prepared at pH 2 exhibited a dominant (101) preferred orientation, whereas increasing the pH to 7 resulted in a shift to a (002) orientation. In the sample prepared at pH 9, the intensity of the (002) peak was further enhanced, whereas at pH 12, a decrease in the intensity of all peaks was observed without an accurate comparison. This situation can be explained by the fact that the amount of ethanolamine used as a stabilizer may affect the stability of the solution. The change from (101) to (002) orientation suggests a transition in the growth dynamics of the ZnO thin film, likely caused by factors such as pH in our case. Therefore, a possible explanation for the growth of the ZnO sample produced at low pH (2) with dominant (101) orientation is the influence of the excess hydrogen ions (H^+) on the structure. Excessive H^+ ions may react with hydroxide ions (OH^-), reducing the OH^- ion concentration required for the formation of the ZnO reaction given in Equation (1).

$$Zn^{2+} + 2OH^- \rightarrow ZnO + H_2O \quad (1)$$

Increasing ethanolamine enhances the stability of ZnO thin films, promoting a preferred orientation of (002) along the c-axis, which is often preferred for optoelectronic applications due to its lowest surface energy and lowest internal stress [35]. This effect is primarily attributed to the proton-releasing nature of ethanolamine and the increase in OH^- ions in the structure. The increase in OH^- ions, which provides a link to Zn-O-Zn bonds, leads to the formation of more Zn-O-Zn chains in the structure, resulting in the (002) orientation [36]. In this context, the expanded view of the three dominant peak variations and the relationship between the relative intensity of $I_{002}/(I_{100} + I_{002} + I_{101})$ with pH value is presented in Figure 1b. As seen in the figure, the relative intensity of the (002) peak increased, reaching its highest point (0.345) at pH 9, and then decreased to a lower level for pH 12. At pH 12 or higher values, the growth mechanism of the ZnO may worsen due to agglomeration and/or over-saturation in the structure which makes crystal growth more difficult. In addition to these, irrespective of the pH value, a c/a value of the samples below 1.633 corresponds to an ideal ZnO hexagonal crystallographic structure [37]. This suggests that all of the samples were faced with in-plane stress, which was potentially due to the mismatch in thermal expansion coefficients between ZnO (7×10^{-6} °C^{-1}) and the glass substrate (9×10^{-6} °C^{-1}) [38].

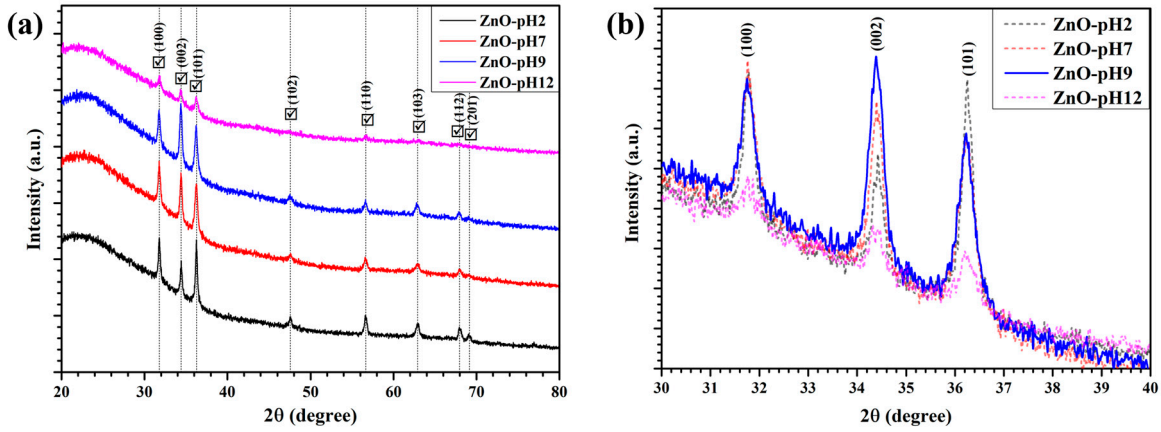


Figure 1. The XRD pattern of ZnO thin films grown at different pH values (**a**) 0–80° (**b**) 30–40°.

The optical properties of ZnO thin films produced at different pH values were characterized via an Ellipsometer. The optical band gap (Eg) values of the films were calculated using the film transmittance (T). The absorption coefficients (α) of the films were determined based on the transmittance values and film thicknesses using Lambert-Beer's law (Equation (2)) [39].

$$\alpha = (\frac{1}{d})\ln(\frac{1}{T}) \quad (2)$$

In this equation, α represents the absorption coefficient, d denotes the thickness of the sample, and T indicates the optical transmittance. Using the absorption coefficients calculated with Equation (2), the band gap values of the thin films were determined [40].

$$(\alpha hv) = A(hv - E_g)^n \quad (3)$$

The band gap values of the thin films are calculated using Equation (3). In this equation, E_g represents the forbidden energy band gap, A is a proportionality constant, and hv denotes the photon energy. The value n indicates the nature of the transition and is 1/2 for direct band gap semiconductors like ZnO. The band gap of the samples is determined by plotting the graph of $(\alpha hv)^2$-(hv) and analyzing the graph to find the band gap value.

Figure 2 shows that the optical transmittance of the samples was 83% for pH 2, 86% for pH 7, and reached the highest value (88%) for pH 9, then sharply decreased to 80% for pH 12. This indicates that all samples have a transmittance of $\geq$80%, which is consistent with the literature. Figure 3 represents the band gap values of the samples produced at different pH levels. It is observed that all ZnO samples have a band gap in the range of 3.42 to 3.55 eV [41].

The figure of merit (FOM) for the samples was determined at each pH value using Equation (4). In this equation, T represents the transmittance at a wavelength of 550 nm, and Rsh denotes the sheet resistance. Figure 4 illustrates the Rsh values and the corresponding FOM values. As shown in the figure, the Rsh value is on the order of 10^5 and increases with rising pH. It is hypothesized that the maximum Rsh value observed at pH 12 results from potential agglomeration and clustering within the film structure, as discussed in previous sections. The high FOM and Rsh values indicate that the optimal production pH is 9 for obtaining an intrinsic ZnO layer with high transmittance and strong insulating properties, making it suitable for use in solar cell structures.

$$FOM = \frac{T^{10}}{R_{sh}} \quad (4)$$

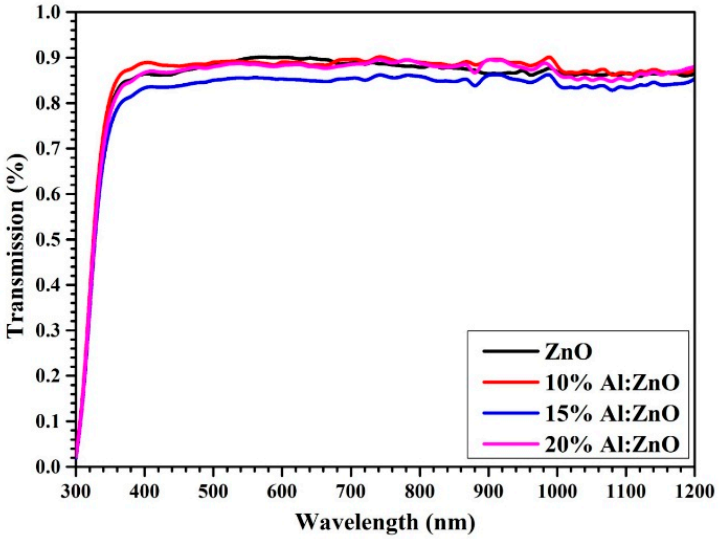


Figure 2. Optical transmittance spectrum of the ZnO samples produced at different pH values.

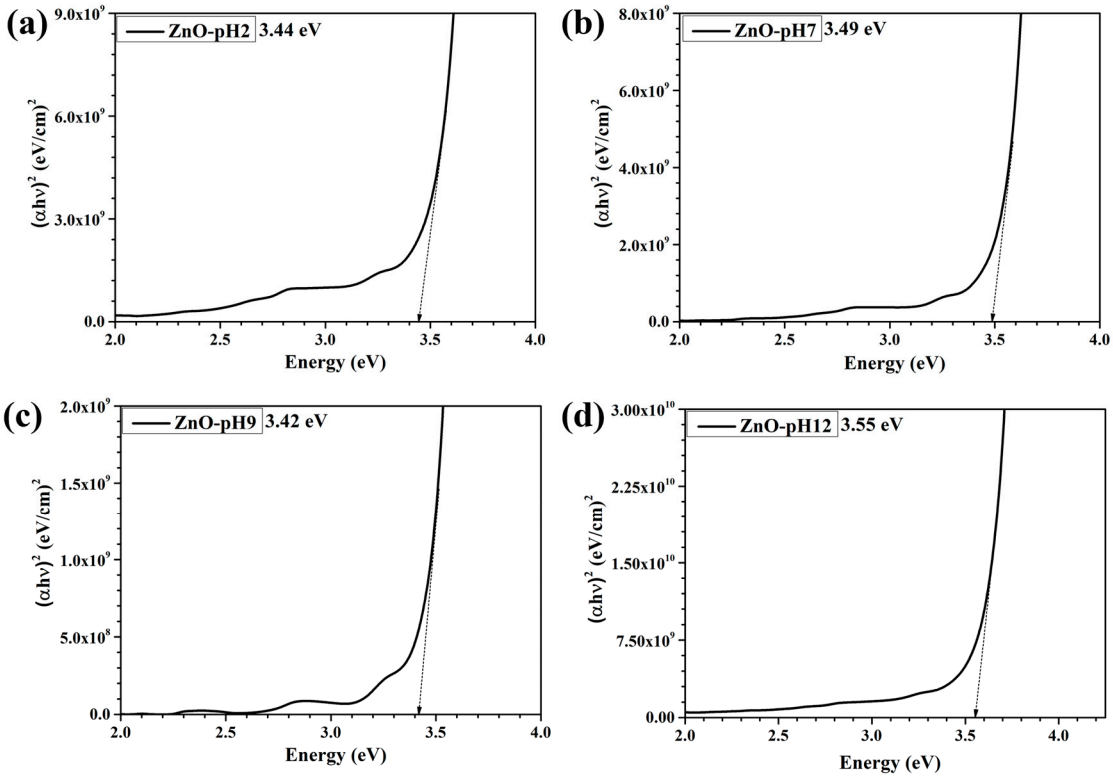


Figure 3. The band gap value determination of the ZnO samples grown at (**a**) pH 2, (**b**) pH 7, (**c**) pH 9, and (**d**) pH 12.

Among the ZnO films produced at various pH levels, the ZnO-pH9 film demonstrated the best performance as a buffer layer in thin-film-based solar cells due to its desirable crystal quality with highly oriented hexagonal phase, a suitable band gap of approximately 3.4 eV, and the highest optical transmittance, which enhances photon entry into the absorber layer and thus to the solar cell [42].

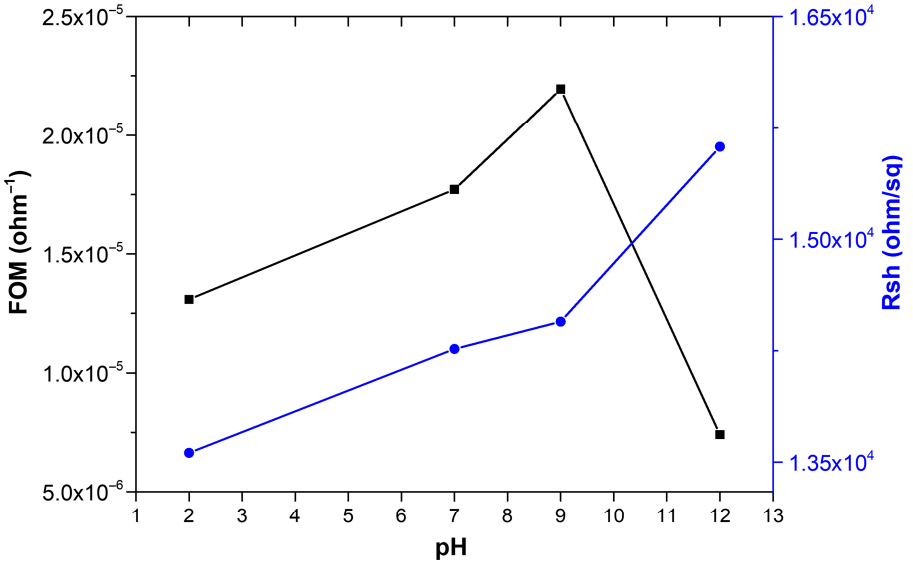


Figure 4. FOM and sheet resistance value of ZnO films produced at different pH values.

Based on these results, the pH value of 9 was chosen for preparing the solution for aluminum-doped zinc oxide films. Table 1 presents the EDX results for AZO samples produced with different doping levels and an undoped ZnO film for comparison. According to the table, the ZnO thin film contains 19.3% Zn and 80.7% O. In addition, the excess oxygen observed in all samples, regardless of the Al content, can be attributed to the natural occurrence of chemical processes. On the other hand, the increased O concentration might be due to the high penetration depth of the X-ray, which could interact with the glass substrate (SiO_2). Still, it was determined that Al doping ratios identified throughout the manuscript were consistent with the target values within the experimental error limits. The presence of Al in the samples suggests that the Al atoms have been successfully integrated into the ZnO matrix.

Table 1. EDX results and some atomic ratios of undoped and Al-doped ZnO films.

Sample	Atomic (%)			Atomic Ratio	
	% Zn	% O	% Al	Zn/O	Al/(Al + Zn)
ZnO	19.3	80.7	-	0.24	-
10%-Al:ZnO	17.1	80.8	2.2	0.21	0.11
15%-Al:ZnO	18.8	77.9	3.3	0.24	0.15
20%-Al:ZnO	17	79.1	3.9	0.22	0.19

The transmittance spectra for undoped and Al-doped ZnO films are shown in Figure 5. According to Figure 5, the undoped ZnO film has an average transmittance of approximately 87% in the visible range (400–800 nm), while the ZnO films with 10%, 15%, and 20% Al doping have transmittance values of 89%, 85%, and 87%, respectively. Figure 6 illustrates the bandgap values for undoped and Al-doped ZnO thin films at various doping levels. The figure shows that the undoped ZnO thin film has a bandgap of 3.46 eV. With Al doping, the bandgap values are observed to be 3.63, 3.56, and 3.60 eV for doping levels of 10%, 15%, and 20%, respectively. Literature also indicates that the bandgap increases with aluminum doping, confirming that the produced samples are consistent with reported values [43]. Overall, ZnO thin films doped with 15% Al exhibited superior properties.

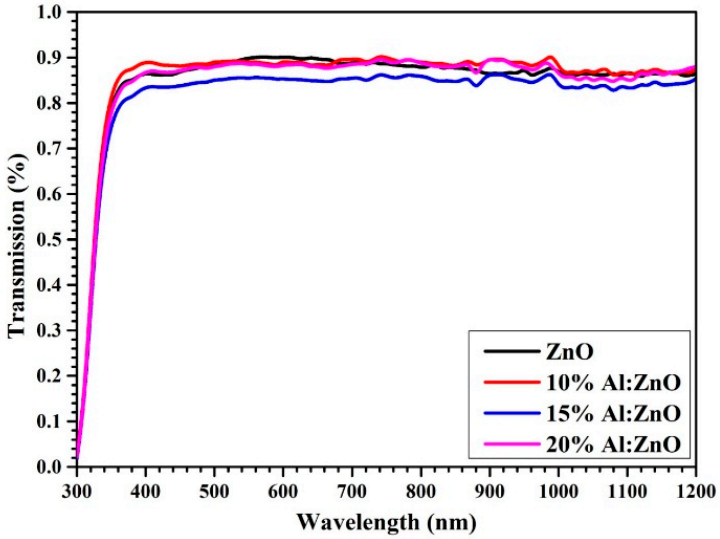


Figure 5. Optical transmittance spectrum of the undoped and Al-doped ZnO samples.

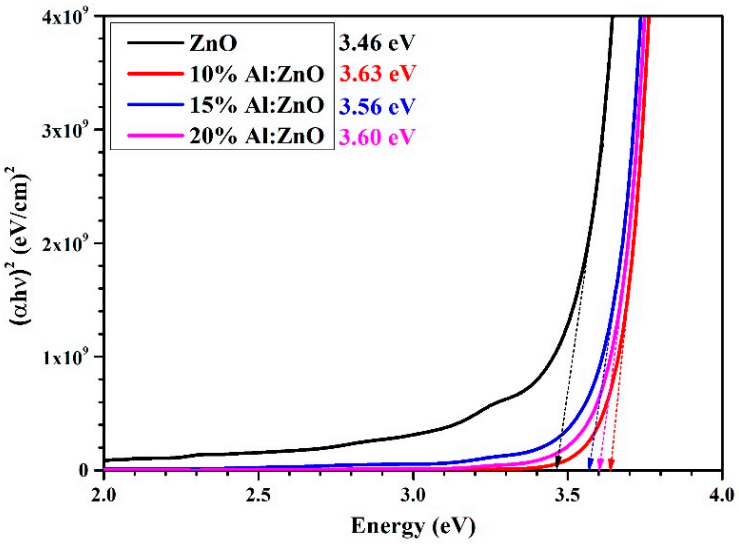


Figure 6. The band gap value determination of the undoped and Al-doped ZnO samples using $(\alpha h\nu)^2$-$(h\nu)$ graph.

Figure 7 shows the photoluminescence (PL) measurements obtained using an excitation wavelength of 280 nm at room temperature. The PL spectra of ZnO and AZO thin films exhibit defect-related emission bands centered at ~420 nm (2.95 eV) and ~435 nm (2.85 eV), which are commonly associated with zinc vacancies (V_{Zn}), oxygen interstitials (O_i), and zinc interstitials (Zn_i). With increasing Al content, a noticeable suppression of the defect-related visible emission relative to the near-band-edge UV emission is observed. In particular, the 15% Al-doped AZO film shows the lowest defect-to-UV emission intensity ratio, indicating a reduced density of radiative defect states. This trend is consistent with improved electrical properties (lower resistivity and higher carrier mobility), suggesting that Al incorporation effectively passivates native defects and enhances crystalline quality.

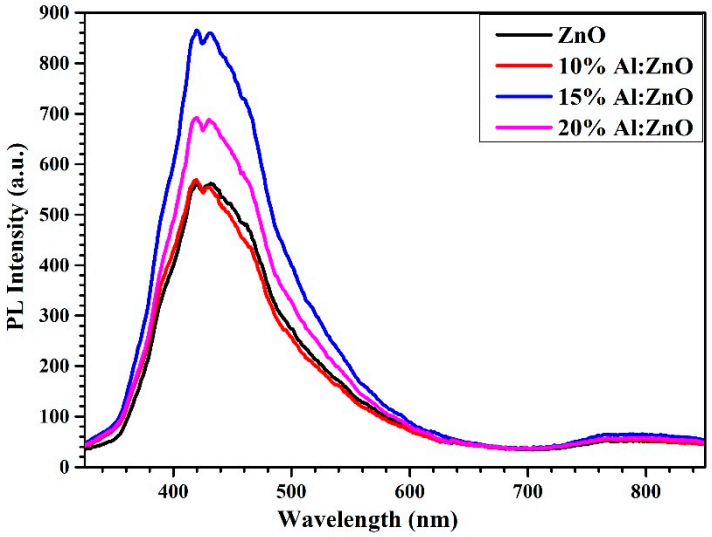


Figure 7. The PL spectrum of the undoped and Al-doped ZnO samples.

3.2. Electrical Measurements

Table 2 summarizes the resistivity, carrier density, and mobility values of undoped and Al-doped ZnO thin films. All samples exhibit n-type electrical conductivity, confirming that Al acts as an effective donor in the ZnO lattice. Compared to undoped ZnO, Al incorporation leads to a significant reduction in resistivity, reaching a minimum value of 1.0×10^3 Ω·cm at 15% Al doping. This improvement is accompanied by a marked increase in carrier concentration, which rises from 2.1×10^{14} cm^{-3} for ZnO to 6.9×10^{14} cm^{-3} at 15% Al doping, as well as a substantial enhancement in carrier mobility [44]. The increase in carrier concentration with Al doping is attributed to the substitution of Zn, which introduces additional free electrons into the ZnO lattice. However, further increasing the Al content to 20% results in a reduction in carrier density and mobility, leading to a higher resistivity. This degradation is likely due to excessive Al incorporation causing defect formation, dopant clustering, or increased carrier scattering, which limits effective donor activation. Consequently, the results indicate that a 15% Al doping level provides the highest carrier concentration and mobility along with the lowest resistivity, yielding the best electrical performance among the investigated samples.'

Table 2. Some electrical parameters of the undoped and Al-doped ZnO samples.

Sample	Resistivity (ohm.cm)	Carrier Density (cm^{-3})	Mobility (cm^2/V.s)
ZnO	$(1.5 \pm 0.7) \times 10^4$	$(2.1 \pm 0.4) \times 10^{14}$	2.2 ± 0.6
10%-Al:ZnO	$(2.6 \pm 2.2) \times 10^3$	$(4.1 \pm 1.2) \times 10^{14}$	4.1 ± 0.5
15%-Al:ZnO	$(1.0 \pm 0.3) \times 10^3$	$(6.9 \pm 0.8) \times 10^{14}$	8.7 ± 0.7
20%-Al:ZnO	$(3.7 \pm 1.3) \times 10^3$	$(4.4 \pm 1.1) \times 10^{14}$	4.3 ± 0.5

Based on these opto-electrical results, the aluminum doping ratio was set at 15% for the preparation of graphene-doped AZO films. Raman spectroscopy analysis was performed to evaluate the structural quality and defect level of the graphene powder obtained via the liquid-phase exfoliation (LPE) method (Figure 8). The Raman spectrum clearly exhibits the characteristic D (~1323 cm^{-1}), G (~1571 cm^{-1}), and 2D (~2689 cm^{-1}) bands of carbon-based materials, confirming the successful exfoliation of graphite into graphene flakes. The weak intensity of the D band, which represents structural disorder, and the resulting low I_D/I_G ratio (~0.155) indicate that the graphene possesses a low defect density and a

well-preserved sp2 carbon network [45]. This low defect level is attributed primarily to edge-related defects rather than basal-plane disorder, which is a typical feature of high-quality LPE graphene with relatively large flake sizes. Furthermore, the lower intensity of the 2D band compared to the G band ($I_{2D}/I_G < 1$) and its broadened profile confirm that the obtained material consists of few-layer graphene rather than monolayer graphene. This few-layer structure provides an optimal balance between dispersion stability in the solvent and electrical conductivity, making it suitable for thin-film applications [46].

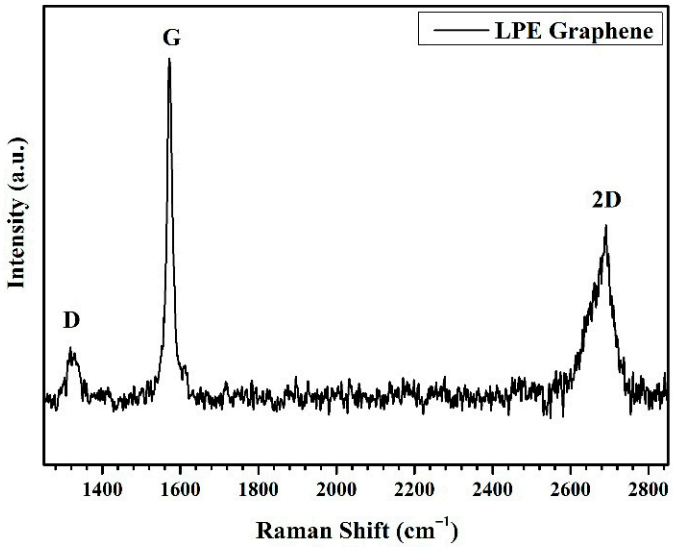


Figure 8. Raman spectrum of LPE graphene.

Graphene powder was added to the AZO solution at concentrations of 0.5%, 1%, 1.5%, and 2%. The XRD patterns of the AZO and Gr:AZO films were presented in Figure 9, confirm that all samples crystallize in a hexagonal wurtzite structure of ZnO and have characteristic diffraction peaks at approximately 31.75°, 34.4°, and 36.22°, corresponding to planes (100), (002), and (101), respectively. Upon Al and Al:Gr doping the main diffraction peaks slightly shifted towards high diffraction angles, as expected in comparison to the ZnO. Within the resolution limits of the XRD measurements, no additional diffraction peaks associated with secondary phases such as Al_2O_3, metallic Al, or graphene-related phases were detected; this indicates that Al ions are successfully incorporated into the ZnO lattice and graphene does not form a separate crystalline phase.

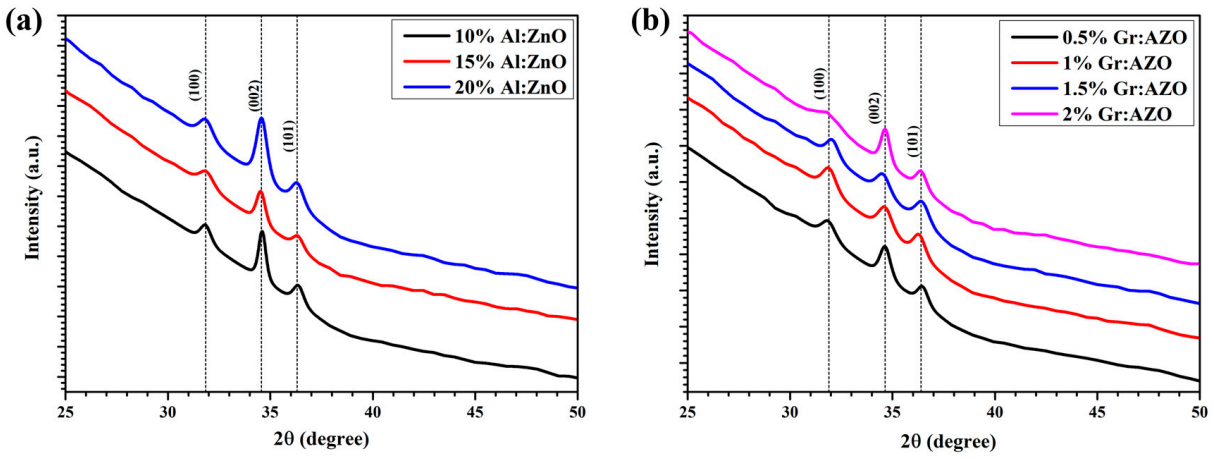


Figure 9. XRD patterns of AZO (**a**) and Gr:AZO (**b**) thin films.

Using the main diffraction peaks corresponding to the (002) orientation of ZnO thin films, several structural parameters were calculated. First, the interplanar spacing (d) was calculated using Bragg's law (Equation (5)) [47].

$$n\lambda = 2d\sin\theta \quad (5)$$

In this equation, n represents the order of diffraction, λ is the wavelength of the incident X-ray radiation, d denotes the interplanar spacing, and θ corresponds to the diffraction angle. Using the d-spacing obtained from Bragg's law, the lattice parameters (*a* and *c*) were calculated for the hexagonal wurtzite structure according to Equation (6) [48].

$$\frac{1}{d^2} = \frac{4}{3}\frac{h^2 + hk + k^2}{a^2} + \frac{l^2}{c^2} \quad (6)$$

In Equation (6); *h*, *k*, and *l* represent the Miller indices, while *a* and *c* denote the lattice parameters. The full width at half maximum (FWHM) values of the ZnO thin films were determined using the main diffraction peaks corresponding to the (002) orientation. Using FWHM values, the crystallite sizes of the films were calculated according to the Debye-Scherrer equation (Equation (7)) [49].

$$D = \frac{K*\lambda}{\beta*\cos\theta} \quad (7)$$

Here, D represents the crystallite size, K is the Debye–Scherrer constant (0.94), and β denotes the FWHM of the diffraction peak corresponding to the (002) preferred orientation. Based on the calculations performed using these equations, the structural parameters of the ZnO, AZO and Gr:AZO samples were determined and summarized in Table 3. As the Al and graphene doping concentration increased, a gradual increase in FWHM values was observed, accompanied by a decrease in crystallite size. This behavior is attributed to the lattice distortion and defect formation induced by the inclusion of the dopant, commonly reported for dopant ZnO systems, especially at relatively high doping concentrations [50]. With Al and Al:Gr doping, the lattice parameters (*a* and *c*) slightly decreased due to the difference in ionic radii between Al (0.53 Å) and Zn (0.74 Å). This substitution of Zn by Al induced minor lattice distortion and the formation of crystal defects [9]. These structural changes are expected to affect the optical and electrical properties of the films and are therefore discussed in relation to the relevant performance results in the following sections.

Table 3. Structural parameters of ZnO, AZO and Gr:AZO thin films.

Sample	2θ (°)	FWHM (°)	D (nm)	Lattice Parameters	
				a **(Å)**	***c*** **(Å)**
ZnO	34.40	0.31	28.01	3.250	5.200
10%-Al:ZnO	34.60	0.36	24.13	3.247	5.181
15%-Al:ZnO	34.52	0.39	22.27	3.246	5.192
20%-Al:ZnO	34.56	0.51	17.03	3.252	5.186
0.5%-Gr:AZO	34.62	0.44	19.75	3.237	5.178
1%-Gr:AZO	34.58	0.49	17.73	3.257	5.184
1.5%-Gr:AZO	34.46	0.43	20.19	3.238	5.201
2%-Gr:AZO	34.62	0.41	21.19	3.245	5.178

As shown in Figure 10, the optical transmittance values of the Gr:AZO thin films are presented. With the increase in graphene doping, the average optical transmittance was observed to decrease to 83%, 81%, 81%, and 77%, respectively. The reduction in transmittance is attributed to the increased light absorption by graphene particles, which reduces transparency [51]. Similarly, Xiayang Yu and colleagues fabricated rGO-AZO thin films using the spin coating method with varying rGO concentrations. As a result, while the undoped film exhibited a transmittance of 93%, they observed that the transmittance decreased to as low as 74% with the incorporation of rGO [32].

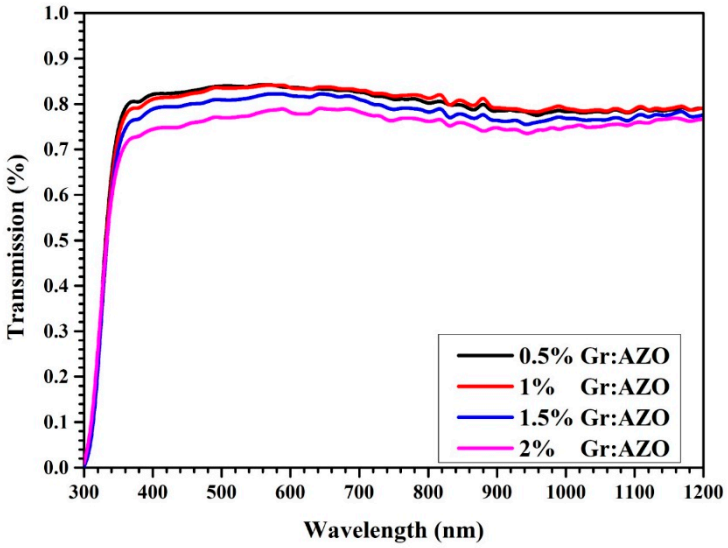


Figure 10. Optical transmittance spectrum of the graphene-doped AZO samples.

The absorption coefficient of the films was calculated based on the transmittance values and the thickness of the produced films using the Lambert-Beer law (Equation (2)). Utilizing the calculated absorption coefficient, the $(\alpha h\nu)^2$-$(h\nu)$ plot was generated for the graphene-doped samples. The results are presented in Figure 11. As seen in the Figure, the optical band gap of the Gr:AZO thin films exhibits a slight reduction compared to AZO, decreasing from 3.52 ± 0.03 eV to a minimum of 3.45 ± 0.03 eV with increasing graphene content. This minor variation is attributed to the suppression of the Burstein–Moss effect due to interfacial charge transfer between graphene and AZO, leading to a reduced free carrier concentration. Additionally, increased structural disorder and defect-induced band tailing at the Gr–AZO interface contribute to the observed band-gap narrowing.

Table 4 presents the resistivity, carrier concentration, and mobility values of Gr:AZO thin films with varying graphene content. All samples exhibit n-type electrical conductivity. The incorporation of graphene leads to an enhancement in carrier concentration, increasing from the order of 10^{14} cm^{-3} at low graphene content to 1.2×10^{15} cm^{-3} at 1.5% Gr doping. This increase is accompanied by a notable improvement in carrier mobility, reaching a maximum value of 13.1 $cm^2/V.s$ at 1.5% Gr, which results in a relatively low resistivity. The improvement in electrical properties at moderate graphene content is attributed to effective charge transfer between graphene and the AZO matrix, as well as improved carrier transport pathways provided by the graphene network [32]. However, further increasing the graphene content to 2% leads to a reduction in both carrier concentration and mobility, accompanied by an increase in resistivity. This degradation is likely due to graphene agglomeration and enhanced carrier scattering at higher doping levels, which limit effective charge transport. Consequently, the results indicate that a graphene doping level of 1.5% provides an optimal balance between carrier concentration and mobility, yielding the best electrical performance among the investigated Gr:AZO films [52].

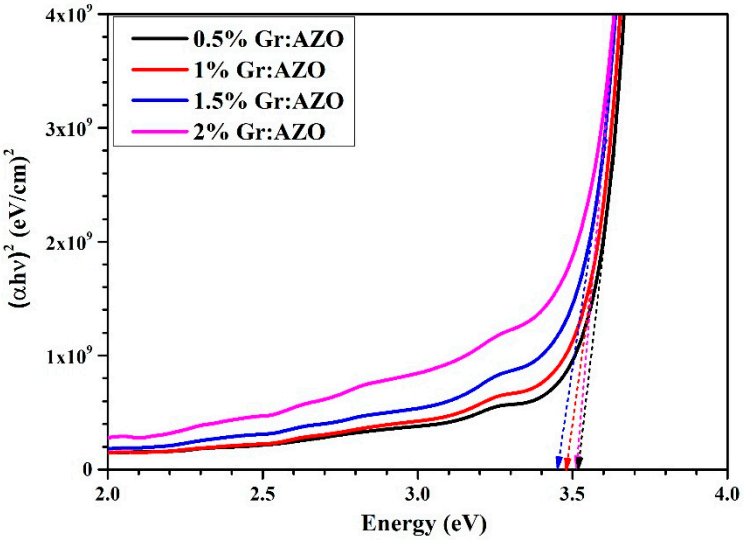


Figure 11. The band gap value determination of the graphene-doped AZO samples using $(\alpha h\nu)^2$-$(h\nu)$ graph.

Table 4. Some electrical parameters of the Gr:AZO samples.

Sample	Resistivity (ohm.cm)	Carrier Density (cm^{-3})	Mobility ($cm^2/V.s$)
0.5%-Gr:AZO	$(5.1 \pm 0.4) \times 10^3$	$(5.1 \pm 3.1) \times 10^{14}$	4.1 ± 0.7
1%-Gr:AZO	$(3.5 \pm 0.2) \times 10^3$	$(5.0 \pm 0.5) \times 10^{14}$	5.0 ± 0.5
1.5%-Gr:AZO	$(4.3 \pm 1.1) \times 10^3$	$(1.2 \pm 0.3) \times 10^{15}$	13.1 ± 0.3
2%-Gr:AZO	$(6.5 \pm 3.3) \times 10^3$	$(2.5 \pm 0.6) \times 10^{14}$	5.9 ± 0.4

Overall, although higher graphene doping leads to reduced optical transmittance, the enhanced electrical properties at 1.5% graphene indicating an optimal balance between optical and electrical properties for optimal device performance. Thus, a solar cell was fabricated using Gr:AZO thin films employing this doping level.

3.3. Characterization of the CTS Absorber Layer

CTS thin films were obtained via PVD using Cu and Sn targets, which were followed by sulfurization. To assess film quality, various structural, optical, and electrical characterizations were performed. Structural analyses were conducted to examine the crystal structure, phase formation, and surface morphology of the CTS films. All obtained findings were analyzed to assess the suitability of the CTS absorber layer for solar cell applications, and the results are presented in Figure 12a–d. The XRD spectrum of the CTS thin film is provided in Figure 12a. As depicted in the figure, a dominant main peak was observed at approximately $2\theta = 28.50°$, and further characteristic peaks were also identified at approximately $2\theta = 32.98°$, 47.34°, and 56.21° (JCPDS-00-019-0412), indicating the formation of the CTS monoclinic phase. In addition to the CTS phase, the presence of the Cu_4SnS_4 phase (JCPDS-98-000-0833) was detected at around $2\theta = 46.38°$. Using the Debye Scherrer formula, the average crystallite size of the thin film was calculated to be 51.49 nm, which is consistent with the previous works [34]. The Raman spectra of CTS thin films are presented in Figure 12b. The Raman peaks corresponding to the monoclinic structure of CTS were identified at 218 cm^{-1}, 257 cm^{-1}, 285 cm^{-1}, 313 cm^{-1}, and 348 cm^{-1}. In addition to the CTS phase, a peak observed around 365 cm^{-1} was attributed to the Cu_4SnS_4 phase. The surface morphology of the CTS (Cu_2SnS_3) thin film shows homogeneously distributed grains in micron and submicron sizes (Figure 12c). The film appears to have a compact structure

with minimal voids, and the grains seem well-connected, indicating good film quality and favorable conditions for carrier transport. Such a surface morphology can also provide good light absorption properties, which is advantageous for optoelectronic applications. The absorption coefficients of the samples were calculated using the Lambert-Beer law based on the transmittance values measured at room temperature in the wavelength range of 300–1350 nm. The $(\alpha h\nu)^2$-$(h\nu)$ plot was generated using Equation (3), and the band gap of the film was determined from the graph. The obtained plot is presented in Figure 12d. Based on the graph, it was observed that the CTS thin film has a band gap value of 0.98 eV.

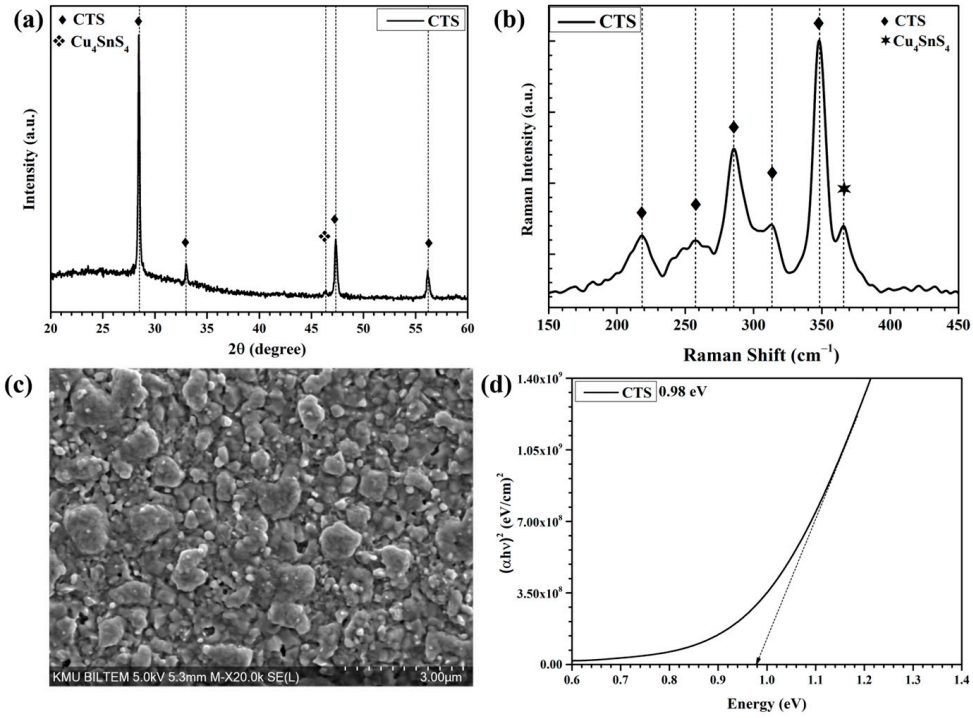


Figure 12. (**a**) XRD spectrum, (**b**) Raman spectrum, (**c**) SEM image, and (**d**) absorption spectrum of CTS thin film.

When the atomic percentages of the elements in the grown CTS film are examined, Cu is seen as 28.9%, Sn as 18.8%, and S as 52.3% as shown in Table 5. According to these percentages, it is concluded that the S/metal ratio is quite close to the stoichiometric value of 1. The Cu/Sn ratio of the CTS film was determined to be 1.54, indicating a Cu-poor composition, which is considered favorable for solar cell applications. Furthermore, the CTS thin film showed p-type conductivity with a carrier density of 3.54×10^{19} cm^{-3} and a resistivity of 1.01×10^{-1} Ω.cm, indicating that it is suitable for photovoltaic applications.

Table 5. EDX results and some atomic ratios of CTS thin-film.

Sample	Atomic (%)			Atomic Ratio	
	Cu	Sn	S	Cu/Sn	S/Metal
CTS	28.9	18.8	52.3	1.54	1.09

3.4. Solar Cell

To evaluate the impact of chemically produced ZnO, AZO and Gr:AZO layers on solar cell device performance, CTS thin-film based solar cell structures were fabricated. Within the scope of this study, initially two solar cells were fabricated: one using ZnO and AZO layers deposited via a PVD system, and the other using ZnO and AZO layers

chemically grown by spin coating to compare the effect of the fabrication approach of the TCO layer. Subsequently, to investigate the effect of graphene incorporation, another cell was fabricated using Gr:AZO.

The performance of these cells was characterized through J-V measurements, as shown in Figure 13. According to the figure, the cell with the configuration glass/Mo/CTS/CdS/ZnO/AZO, where the layers were deposited using the PVD system, exhibited an open-circuit voltage (V_{oc}) of 0.257 V, a short-circuit current density (J_{sc}) of 20.41 mA/cm^2, a fill factor (FF) of 0.36, and a power conversion efficiency (PCE) of approximately 1.88%. In contrast, the cell structure using ZnO and AZO layers grown via chemical methods with the configuration glass/Mo/CTS/CdS/ZnO/AZO yielded a V_{oc} of 0.236 V, a J_{sc} of 20.89 mA/cm^2, an FF of 0.35, and a PCE of approximately 1.72%. The cell with the configuration glass/Mo/CTS/CdS/ZnO/Gr:AZO demonstrated a V_{oc} of 0.173 V, a J_{sc} of 28.96 mA/cm^2, an FF of 0.40, and a PCE of approximately 2.02%. Graphene incorporation clearly enhanced the cell efficiency by increasing the carrier density within the TCO layer. This improvement can be attributed to graphene's excellent electrical conductivity and high carrier mobility, which facilitate more efficient charge transport and reduce resistive losses in the device. Although Gr:AZO improves carrier transport and enhances Jsc, the accompanying Fermi-level shift and possible conduction band misalignment at the CdS/ZnO interface promote interfacial recombination, resulting in a reduced Voc.

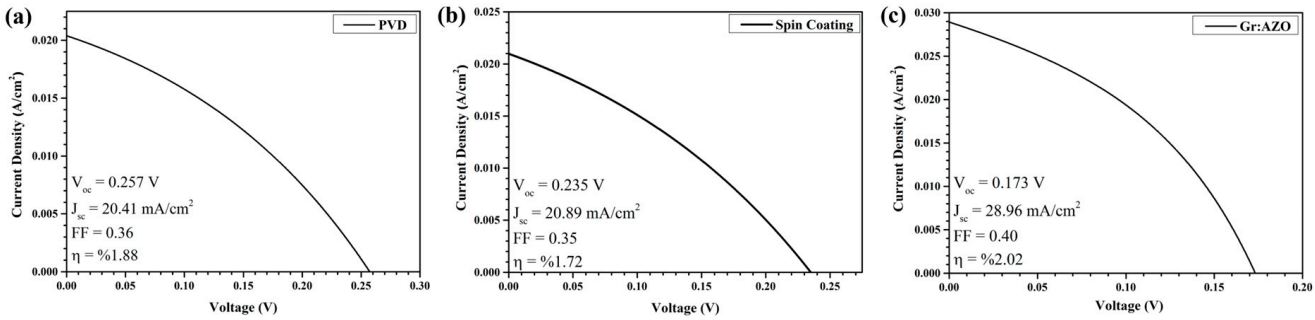


Figure 13. J-V measurements of the cell ZnO and AZO obtained with (**a**) PVD, (**b**) Spin Coating, and (**c**) Gr:AZO.

4. Conclusions

In conclusion, this study successfully demonstrated the development of ZnO-based transparent conducting oxide (TCO) layers with improved optoelectronic properties through a cost-effective and environmentally friendly approach via Al and graphene doping. The optimization of synthesis parameters revealed that a pH level of 9 and an Al doping concentration of 15% resulted in the most favorable structural, optical, and electrical characteristics. Further enhancement was achieved by incorporating graphene into the optimized AZO structure at 1.5%, yielding a Gr:AZO film with superior TCO performance. When employed as TCO layers in CTS-based thin-film solar cells, the PVD-deposited AZO exhibited the highest conversion efficiency (1.88%), whereas solution-processed AZO delivered slightly lower performance (1.72%). Notably, the incorporation of graphene into the AZO layer improved the efficiency to 2.02%, thereby demonstrating the beneficial role of co-doping in advancing device performance. Overall, these results confirm the promising potential of Gr:AZO thin films as alternative, solution-processable TCO layers, offering both cost-effectiveness and performance improvements for next-generation thin-film solar cell technologies.

Author Contributions: D.O.: Sample preparation, Characterization, Writing—original draft. M.C.: Sample preparation. G.T.: Sample preparation. S.E. (Sevde Erkan): Characterization. S.E. (Serkan Erkan): Characterization. A.A.: Characterization K.O.: Writing—review & editing. S.A.: Writing—review & editing. Y.A.: Characterization, Writing—original draft. M.A.O.: Methodology, Writing—review & editing. R.Z.: Conceptualization, Methodology, Characterization, Writing—review & editing. All authors have read and agreed to the published version of the manuscript.

Funding: This research was funded by The Scientific and Technological Research Council of Türkiye (TUBITAK) under a project number of 122F217.

Data Availability Statement: The data supporting the findings of this study are available from the corresponding author upon reasonable request.

Conflicts of Interest: The authors declare no competing interests.

References

1. Rosa, A.; Da Silva, E.; Amorim, E.; Chaves, M.; Catto, A.; Lisboa-Filho, P.N.; Bortoleto, J. Growth evolution of ZnO thin films deposited by RF magnetron sputtering. *J. Phys. Conf. Ser.* **2012**, *370*, 012020. [CrossRef]
2. Zan, R.; Olgar, M.A.; Altuntepe, A.; Seyhan, A.; Turan, R. Integration of graphene with GZO as TCO layer and its impact on solar cell performance. *Renew. Energy* **2022**, *181*, 1317–1324. [CrossRef]
3. Myzaferi, A.; Reading, A.; Cohen, D.; Farrell, R.; Nakamura, S.; Speck, J.; DenBaars, S. Transparent conducting oxide clad limited area epitaxy semipolar III-nitride laser diodes. *Appl. Phys. Lett.* **2016**, *109*, 061109. [CrossRef]
4. Chu, S.; Olmedo, M.; Yang, Z.; Kong, J.; Liu, J. Electrically pumped ultraviolet ZnO diode lasers on Si. *Appl. Phys. Lett.* **2008**, *93*, 181106. [CrossRef]
5. Liu, P.-T.; Chou, Y.-T.; Teng, L.-F. Charge pumping method for photosensor application by using amorphous indium-zinc oxide thin film transistors. *Appl. Phys. Lett.* **2009**, *94*, 242101. [CrossRef]
6. Jun, K.H.; Bunte, E.; Stiebig, H. Optimization of phase-sensitive transparent detector for length measurements. *IEEE Trans. Electron. Devices* **2005**, *52*, 1656–1661. [CrossRef]
7. Lim, J.H.; Kang, C.K.; Kim, K.K.; Park, I.K.; Hwang, D.K.; Park, S.J. UV electroluminescence emission from ZnO light-emitting diodes grown by high-temperature radiofrequency sputtering. *Adv. Mater.* **2006**, *18*, 2720–2724. [CrossRef]
8. Wang, H.; Xu, M.-H.; Xu, J.-W.; Ren, M.-F.; Yang, L. Low temperature synthesis of sol–gel derived Al-doped ZnO thin films with rapid thermal annealing process. *J. Mater. Sci. Mater. Electron.* **2010**, *21*, 589–594. [CrossRef]
9. Altuntepe, A.; Erkan, S.; Hasret, O.; Yagmyrov, A.; Yazici, D.; Tomakin, M.; Olgar, M.A.; Zan, R. Performance of Si-based solar cell utilizing optimized Al-doped ZnO films as TCO layer. *J. Mater. Sci. Mater. Electron.* **2023**, *34*, 75. [CrossRef]
10. Hasim, S.N.F.; Hamid, M.A.A.; Shamsudin, R.; Jalar, A. Synthesis and characterization of ZnO thin films by thermal evaporation. *J. Phys. Chem. Solids* **2009**, *70*, 1501–1504. [CrossRef]
11. Sun, Y.; Fuge, G.M.; Ashfold, M.N. Growth of aligned ZnO nanorod arrays by catalyst-free pulsed laser deposition methods. *Chem. Phys. Lett.* **2004**, *396*, 21–26. [CrossRef]
12. Kim, S.; Jeong, M.-C.; Oh, B.-Y.; Lee, W.; Myoung, J.-M. Fabrication of Zn/ZnO nanocables through thermal oxidation of Zn nanowires grown by RF magnetron sputtering. *J. Cryst. Growth* **2006**, *290*, 485–489. [CrossRef]
13. Mahmood, A.; Ahmed, N.; Raza, Q.; Khan, T.M.; Mehmood, M.; Hassan, M.; Mahmood, N. Effect of thermal annealing on the structural and optical properties of ZnO thin films deposited by the reactive e-beam evaporation technique. *Phys. Scr.* **2010**, *82*, 065801. [CrossRef]
14. Yılmaz, S.; Parlak, M.; Özcan, Ş.; Altunbaş, M.; McGlynn, E.; Bacaksız, E. Structural, optical and magnetic properties of Cr doped ZnO microrods prepared by spray pyrolysis method. *Appl. Surf. Sci.* **2011**, *257*, 9293–9298. [CrossRef]
15. Farrag, A.A.-G.; Balboul, M.R. Nano ZnO thin films synthesis by sol–gel spin coating method as a transparent layer for solar cell applications. *J. Sol-Gel Sci. Technol.* **2017**, *82*, 269–279. [CrossRef]
16. Naseri, M.; Fotouhi, L.; Ehsani, A.; Shiri, H.M. Novel electroactive nanocomposite of POAP for highly efficient energy storage and electrocatalyst: Electrosynthesis and electrochemical performance. *J. Colloid Interface Sci.* **2016**, *484*, 308–313. [CrossRef]
17. Taunk, P.; Das, R.; Bisen, D.; Tamrakar, R.; Rathor, N. Synthesis and optical properties of chemical bath deposited ZnO thin film. *Karbala Int. J. Mod. Sci.* **2015**, *1*, 159–165. [CrossRef]
18. Siahsahlan, M.; Aref, S.M.; Naghshara, H. Structural and optical properties of ZnO thin films as a function of pH value and its effect on photoelectrochemical water splitting. *Phys. Scr.* **2024**, *99*, 055533. [CrossRef]
19. Abdulrahman, A.F.; Ahmed, S.M.; Hamad, S.M.; Almessiere, M.A.; Ahmed, N.M.; Sajadi, S.M. Effect of different pH values on growth solutions for the ZnO nanostructures. *Chin. J. Phys.* **2021**, *71*, 175–189. [CrossRef]

20. Meziane, K.; El Hichou, A.; El Hamidi, A.; Mansori, M.; Liba, A.; Almaggoussi, A. On the sol pH and the structural, optical and electrical properties of ZnO thin films. *Superlattices Microstruct.* **2016**, *93*, 297–302. [CrossRef]
21. Nosidlak, N.; Jaglarz, J.; Dulian, P.; Pietruszka, R.; Witkowski, B.S.; Godlewski, M.; Powroźnik, W.; Stapiński, T. The thermo-optical and optical properties of thin ZnO and AZO films produced using the atomic layer deposition technology. *J. Alloys Compd.* **2022**, *900*, 163313. [CrossRef]
22. Sandeep, K.; Bhat, S.; Dharmaprakash, S. Structural defects and photoluminescence studies of sol–gel prepared ZnO and Al-doped ZnO films. *Appl. Phys. A* **2016**, *122*, 975. [CrossRef]
23. Lin, Y.-S.; Lien, S.-Y.; Huang, Y.-C.; Wang, C.-C.; Liu, C.-Y.; Nautiyal, A.; Wuu, D.-S.; Lee, S.-J. Effect of oxygen to argon flow ratio on the properties of Al-doped ZnO films for amorphous silicon thin film solar cell applications. *Thin Solid Film.* **2013**, *529*, 50–53. [CrossRef]
24. Yılmaz, S.; Polat, İ.; Atasoy, Y.; Bacaksız, E. Structural, morphological, optical and electrical evolution of spray deposited ZnO rods co-doped with indium and sulphur atoms. *J. Mater. Sci. Mater. Electron.* **2014**, *25*, 1810–1816. [CrossRef]
25. Young, S.-J.; Yang, C.-C.; Lai, L.-T. growth of Al-, Ga-, and In-doped ZnO nanostructures via a low-temperature process and their application to field emission devices and ultraviolet photosensors. *J. Electrochem. Soc.* **2016**, *164*, B3013. [CrossRef]
26. Potter, D.B.; Powell, M.J.; Parkin, I.P.; Carmalt, C.J. Aluminium/gallium, indium/gallium, and aluminium/indium co-doped ZnO thin films deposited via aerosol assisted CVD. *J. Mater. Chem. C* **2018**, *6*, 588–597. [CrossRef]
27. Zi-qiang, X.; Hong, D.; Yan, L.; Hang, C. Al-doping effects on structure, electrical and optical properties of c-axis-orientated ZnO: Al thin films. *Mater. Sci. Semicond. Process.* **2006**, *9*, 132–135. [CrossRef]
28. Mridha, S.; Basak, D. Aluminium doped ZnO films: Electrical, optical and photoresponse studies. *J. Phys. D Appl. Phys.* **2007**, *40*, 6902. [CrossRef]
29. Saadi, H.; Benzarti, Z.; Mourad, S.; Sanguino, P.; Hadouch, Y.; Mezzane, D.; Abdelmoula, N.; Khemakhem, H. Electrical conductivity improvement of (Fe + Al) co-doped ZnO nanoparticles for optoelectronic applications. *J. Mater. Sci. Mater. Electron.* **2022**, *33*, 8065–8085. [CrossRef]
30. Sang, M.; Shin, J.; Kim, K.; Yu, K.J. Electronic and thermal properties of graphene and recent advances in graphene based electronics applications. *Nanomaterials* **2019**, *9*, 374. [CrossRef]
31. Chang, H.; Wu, H. Graphene-based nanomaterials: Synthesis, properties, and optical and optoelectronic applications. *Adv. Funct. Mater.* **2013**, *23*, 1984–1997. [CrossRef]
32. Yu, X.; Xu, J.; Lu, H.; Fang, G. Sol-gel derived Al-doped zinc oxide–Reduced graphene oxide nanocomposite thin films. *J. Alloys Compd.* **2017**, *699*, 79–86. [CrossRef]
33. Bu, I.Y. Highly conductive and transparent reduced graphene oxide/aluminium doped zinc oxide nanocomposite for the next generation solar cell applications. *Opt. Mater.* **2013**, *36*, 299–303. [CrossRef]
34. Olgar, M. Improvement in the structural and optical properties of Cu_2SnS_3 (CTS) thin films through soft-annealing treatment. *Superlattices Microstruct.* **2020**, *138*, 106366. [CrossRef]
35. Bacaksiz, E.; Aksu, S.; Yılmaz, S.; Parlak, M.; Altunbaş, M. Structural, optical and electrical properties of Al-doped ZnO microrods prepared by spray pyrolysis. *Thin Solid Film.* **2010**, *518*, 4076–4080. [CrossRef]
36. Ebrahimifard, R.; Abdizadeh, H.; Golobostanfard, M.R. Controlling the extremely preferred orientation texturing of sol–gel derived ZnO thin films with sol and heat treatment parameters. *J. Sol-Gel Sci. Technol.* **2020**, *93*, 28–35. [CrossRef]
37. O'Keeffe, M.; Hyde, B.G. *Crystal Structures*; Courier Dover Publications: Garden City, NY, USA, 2020.
38. Bacaksiz, E.; Parlak, M.; Tomakin, M.; Özçelik, A.; Karakız, M.; Altunbaş, M. The effects of zinc nitrate, zinc acetate and zinc chloride precursors on investigation of structural and optical properties of ZnO thin films. *J. Alloys Compd.* **2008**, *466*, 447–450. [CrossRef]
39. Zan, R.; Olgar, M.A.; Atasoy, Y.; Erkan, S.; Altuntepe, A. Boron doped graphene and MoS2 based ultra-thin Schottky junction solar cell. *Opt. Mater.* **2025**, *162*, 116828. [CrossRef]
40. Tauc, J. Optical properties and electronic structure of amorphous Ge and Si. *Mater. Res. Bull.* **1968**, *3*, 37–46. [CrossRef]
41. Kumar, S.; Jeon, H.; Kang, T.; Seth, R.; Panwar, S.; Shinde, S.K.; Waghmode, D.; Saratale, R.G.; Choubey, R.K. Variation in chemical bath pH and the corresponding precursor concentration for optimizing the optical, structural and morphological properties of ZnO thin films. *J. Mater. Sci. Mater. Electron.* **2019**, *30*, 17747–17758. [CrossRef]
42. Salam, S.; Islam, M.; Akram, A. Sol–gel synthesis of intrinsic and aluminum-doped zinc oxide thin films as transparent conducting oxides for thin film solar cells. *Thin Solid Film.* **2013**, *529*, 242–247. [CrossRef]
43. Kars Durukan, I.; Özen, Y.; Kizilkaya, K.; Öztürk, M.; Memmedli, T.; Özçelik, S. Effects of annealing and deposition temperature on the structural and optical properties of AZO thin films. *J. Mater. Sci. Mater. Electron.* **2013**, *24*, 142–147. [CrossRef]
44. Al-Ghamdi, A.A.; Al-Hartomy, O.A.; El Okr, M.; Nawar, A.; El-Gazzar, S.; El-Tantawy, F.; Yakuphanoglu, F. Semiconducting properties of Al doped ZnO thin films. *Spectrochim. Acta Part A Mol. Biomol. Spectrosc.* **2014**, *131*, 512–517. [CrossRef]

45. Hadi, A.; Zahirifar, J.; Karimi-Sabet, J.; Dastbaz, A. Graphene nanosheets preparation using magnetic nanoparticle assisted liquid phase exfoliation of graphite: The coupled effect of ultrasound and wedging nanoparticles. *Ultrason. Sonochem.* **2018**, *44*, 204–214. [CrossRef]
46. Ferrari, A.C.; Meyer, J.C.; Scardaci, V.; Casiraghi, C.; Lazzeri, M.; Mauri, F.; Piscanec, S.; Jiang, D.; Novoselov, K.S.; Roth, S. Raman spectrum of graphene and graphene layers. *Phys. Rev. Lett.* **2006**, *97*, 187401. [CrossRef] [PubMed]
47. Cullity, B.; Stock, S. *Elements of X-Ray Diffraction*, 3rd ed.; Prentice Hall: Hoboken, NJ, USA, 2001; pp. 174–177.
48. Aryanto, D.; Jannah, W.; Sudiro, T.; Wismogroho, A.; Sebayang, P.; Marwoto, P. Preparation and structural characterization of ZnO thin films by sol-gel method. *J. Phys. Conf. Ser.* **2017**, *817*, 012025. [CrossRef]
49. Mustapha, S.; Ndamitso, M.; Abdulkareem, A.; Tijani, J.; Shuaib, D.; Mohammed, A.; Sumaila, A. Comparative study of crystallite size using Williamson-Hall and Debye-Scherrer plots for ZnO nanoparticles. *Adv. Nat. Sci. Nanosci. Nanotechnol.* **2019**, *10*, 045013. [CrossRef]
50. Sirirak, R.; Phettakua, P.; Rangdee, P.; Boonruang, C.; Klinbumrung, A. Unveiling the impact of excessive dopant content on morphology and optical defects in carbonation synthesis of nanostructured Al-doped ZnO. *Powder Technol.* **2024**, *435*, 119444. [CrossRef]
51. Nair, R.R.; Blake, P.; Grigorenko, A.N.; Novoselov, K.S.; Booth, T.J.; Stauber, T.; Peres, N.M.; Geim, A.K. Fine structure constant defines visual transparency of graphene. *Science* **2008**, *320*, 1308. [CrossRef] [PubMed]
52. Chou, C.-T.; Wang, F.-H.; Chen, W.-C. Effects of concentration of reduced graphene oxide on properties of sol–gel prepared Al-doped zinc oxide thin films. *Thin Solid Film.* **2016**, *605*, 143–148. [CrossRef]

Disclaimer/Publisher's Note: The statements, opinions and data contained in all publications are solely those of the individual author(s) and contributor(s) and not of MDPI and/or the editor(s). MDPI and/or the editor(s) disclaim responsibility for any injury to people or property resulting from any ideas, methods, instructions or products referred to in the content.